Compact Difference Methods
for Discharge Modeling in Aerodynamics

Jonathan Poggie*

Air Force Research Laboratory, Wright-Patterson AFB, Ohio 45433-7512 USA

This paper explores the feasibility of applying high-order, compact difference methods to the modeling of glow discharges for high-speed flow control. Previous papers (AIAA 2008-1357) have successfully applied second-order finite difference methods to glow discharge modeling. Detailed grid resolution studies, however, have revealed that very fine grid resolution is required for acceptable quantitative results. High-order compact difference methods offer a possible means of achieving high spatial accuracy on coarser grids, potentially leading to a significant reduction in the computational cost of an accurate solution. In previous work (AIAA 2009-1047), preliminary, one-dimensional compact difference calculations were carried out for glow discharge problems. Here the work is extended to two dimensions. Sample compact difference calculations are presented for several test cases, including a Poisson equation solution, a compressible Couette flow problem, a hypersonic laminar boundary layer flow, and a transient plasma-sheath problem. Spatial convergence of second- through sixth-order compact schemes was investigated, and found to be comparable to the theoretical order of accuracy. In particular, compact difference methods of up to sixth order can successfully achieve their theoretical order of accuracy for the coupled Poisson and Euler equations with source terms. Compact difference schemes appear to be a promising numerical approach for modeling plasma actuators for high-speed flow control.

I. Introduction

Since the mid-1990s, there has been considerable research interest in plasma-based flow control techniques for aerospace applications. Because of their favorable weight and power consumption properties, small-scale actuators based on glow and arc discharges have become increasingly popular, and much effort has been invested in numerical modeling of actuator behavior.[1–3]

Toward this end, the author has developed a second-order accurate, finite-difference code capable of modeling the region of finite space-charge present in the vicinity of electrode surfaces in the electric discharges used for flow control.[3–5] The physical model includes the fluid conservation laws for the bulk gas flow, a model for charged particle motion, and a self-consistent computation of the electric potential. This code has been successfully applied to a variety of discharge problems, including low-density plasma-sheath problems, DC glow discharges, and RF glow discharges. Comparisons among different numerical methods have been carried out, and a central difference scheme, an upwind scheme, and a finite difference implementation of the Sharfetter-Gummel scheme have all been found to give very similar results.

Recently, an investigation was carried out on spatial resolution issues in modeling DC glow discharges.[4, 5] A detailed grid resolution study was carried out, and very fine grid resolution was found to be required for acceptable quantitative results. Coarse grids led to underestimates of number density, temperature, and current density and to overestimates of the lateral extent of the discharge column.

High-order compact difference methods[6, 7] offer a possible means of achieving high spatial accuracy on coarser grids, potentially leading to a significant reduction in computational cost. In previous work,[8] preliminary, one-dimensional compact difference calculations were carried out for glow discharge problems. Here the work is extended to two dimensions. Sample compact difference calculations are presented here for several test cases, including a Poisson equation solution, a compressible Couette flow problem, a hypersonic laminar

American Institute of Aeronautics and Astronautics

boundary layer flow, and a transient plasma-sheath problem. Accuracy is evaluated for second- through sixth-order compact schemes, and compared to standard second-order upwind schemes.

II.   Methods

The physical model and the numerical methods are described in this section. The physical model includes the fluid conservation laws for the motion of each species and a self-consistent computation of the electric potential. The baseline numerical implementation involves compact spatial differences of up to sixth order accuracy, driven by a low-storage, fourth-order Runge-Kutta time marching scheme.

A.   Physical Model

Continuum methods, based on moments of the Boltzmann equation, have been a popular and productive means of modeling electrical discharges. One-dimensional modeling of direct-current glow discharges was carried out as early as the late 1950s,[9, 10] and two-dimensional simulations were first carried out in the late 1980s.[11, 12] By the early 1990s, two dimensional simulations of radio-frequency glow discharges[13, 14] and transient low-density discharges[15, 16] had been performed. Three-dimensional simulations have appeared more recently.[3, 17]

A variety of physical models have been employed in such work. One of the most common models is drift-diffusion, assuming local equilibrium with the electric field, so that the transport and ionization coefficients are a function of the local reduced field E/N.[9, 11, 12] The next step up in generality is to solve the electron energy equation as well, and use the local electron temperature T_e instead of the local E/N to determine the coefficients.[18, 19]

Some studies have used continuity-momentum equations in place of the drift-diffusion model, thus including the effects of particle momentum. The role of inertia in DC and RF discharges has been examined, including the momentum of the electrons,[20] the heavy particles,[21] or both.[22, 23] Ion inertia is important in the transient sheath that appears in plasma-source ion implantation,[24] and in modeling the low-density plasma-sheath transition.[25, 26]

One aim of this ongoing project is to determine limits of the moment method in modeling electrical discharges, specifically whether a three-moment model for each species can be accurate and computationally tractable. A relatively general formulation of the conservation equations for electrical discharges is outlined below, based on standard references.[27–29] Briefly, the conservation laws can be derived from moments of the Boltzmann equation, with closure models utilized for the inelastic collision source terms,[29] the elastic collision source terms,[29, 30] and the flux terms.[28, 31, 32]

1.   Governing Equations

The problem of sheath structure in ionized argon was used as a test case in the current project. Gravity is neglected, and the absence of an applied magnetic field is assumed. The conservation equations for each species are:

$$\frac{\partial}{\partial t}\left(m_s n_s\right) + \nabla\cdot\left(m_s n_s \mathbf{v}_s\right) = S_s$$

$$\frac{\partial}{\partial t}\left(m_s n_s \mathbf{v}_s\right) + \nabla\cdot\left(m_s n_s \mathbf{v}_s \mathbf{v}_s + p_s \mathbf{I}\right) = \nabla\cdot\tau_s + q_s n_s \mathbf{E} + \mathbf{A}_s \tag{1}$$

$$\frac{\partial}{\partial t}\left[m_s n_s\left(\epsilon_s + \tfrac{1}{2}v_s^2\right)\right] + \nabla\cdot\left[m_s n_s \mathbf{v}_s\left(\epsilon_s + \tfrac{1}{2}v_s^2\right) + p_s \mathbf{v}_s\right] = \nabla\cdot\left[\tau_s\cdot\mathbf{v}_s - \mathbf{Q}_s\right] + q_s n_s \mathbf{v}_s\cdot\mathbf{E} + M_s$$

where the notation $s = n, i, e$ indicates the neutrals, ions, and electrons, respectively.

The mass per particle of each species is denoted as m_s, and the corresponding charge per particle is $q_n = 0$, $q_i = +e$, and $q_e = -e$. The number density is n_s, the velocity is $\mathbf{v}_s$, and the translational temperature is T_s. The electric field is $\mathbf{E}$, and the symbol k_B indicates the Boltzmann constant. The pressure is found from $p_s = n_s k_B T_s$, and the internal energy per particle is assumed to have the form $m_s\epsilon_s = H_s + k_B T_s/(\gamma_s - 1)$, where $\gamma_s = 5/3$ is the ratio of specific heats. The heat of formation is $H_n = H_e = 0$ and $H_i = \mathcal{H}$, where $\mathcal{H} = 15.7$ eV for argon ionization.

American Institute of Aeronautics and Astronautics

It assumed that the gas is weakly ionized, so that the primary elastic collisions are with neutral particles. For the inelastic collisions, it is assumed that the species appear or disappear with the average momentum and energy of their peers, except for the electrons, which lose energy $\mathcal{H}$ in each inelastic collision.

The net production rate ω of charged particles in argon gas was given by:

$$\omega = k_f n_n n_e - k_b n_i n_e$$
$$k_f = \sigma_T \sqrt{\frac{8 k_B T_e}{\pi m_e}} \left(1 + \frac{E_i}{k_B T_e}\right) \exp\left(-\frac{E_i}{k_B T_e}\right) \tag{2}$$

with $\sigma_T = 2 \times 10^{-12}$ m^2, $E_i = 15.7$ eV, $k_b = 3.5 \times 10^{-14}$ m^3/s. The ionization rate is from Meyyappan and Kreskovsky[22] and the recombination rate is from Adamovich et al.[33] The species source terms become:

$$S_i = m_i \omega$$
$$S_e = m_e \omega \tag{3}$$
$$S_n = -m_n \omega$$

The momentum source terms are:

$$\mathbf{A}_i = \omega m_i \mathbf{v}_i - n_i m_{in} \nu_{in} (\mathbf{v}_i - \mathbf{v}_n)$$
$$\mathbf{A}_e = \omega m_e \mathbf{v}_e - n_e m_{en} \nu_{en} (\mathbf{v}_e - \mathbf{v}_n) \tag{4}$$
$$\mathbf{A}_n = -(\mathbf{A}_i + \mathbf{A}_e)$$

The collision frequency between the charged and neutral species ν_{sn} was estimated from mobility data, with the correlations for ion and electron mobility in argon taken from Ward.[10] The energy source terms are:

$$M_i = \omega \left(\mathcal{H} + \frac{k_B T_i}{\gamma_i - 1} + \tfrac{1}{2} m_i v_i^2\right) - \frac{n_i m_{in} \nu_{in}}{m_i + m_n} \left[3 k_B (T_i - T_n) + (\mathbf{v}_i - \mathbf{v}_n) \cdot (m_i \mathbf{v}_i + m_n \mathbf{v}_n)\right]$$
$$M_e = \omega \left(-\mathcal{H} + \frac{k_B T_e}{\gamma_e - 1} + \tfrac{1}{2} m_e v_e^2\right) - \frac{n_e m_{en} \nu_{en}}{m_e + m_n} \left[3 k_B (T_e - T_n) + (\mathbf{v}_e - \mathbf{v}_n) \cdot (m_e \mathbf{v}_e + m_n \mathbf{v}_n)\right] \tag{5}$$
$$M_n = -(M_i + M_e)$$

For the neutral particles, it was assumed that the viscous term had a Newtonian form, with Stokes hypothesis applied, and that the heat flux followed Fourier's law:[34]

$$\tau_n = \mu_{vn} \left[(\nabla \mathbf{v}_n) + (\nabla \mathbf{v}_n)^T - \tfrac{2}{3} \nabla \cdot \mathbf{v}_n \mathbf{I}\right]$$
$$\mathbf{Q}_n = -k_n \nabla T_n \tag{6}$$

where μ_{vn} is the viscosity and k_n is the thermal conductivity for the neutral particles. The viscosity and thermal conductivity of the charged particles were neglected for the present work.

To complete the physical model, the electric field must be found from a consistent solution of Maxwell's equations. For the present work, the Poisson equation was solved for the electric potential:

$$\nabla^2 \phi = -\frac{e}{\epsilon_0} (n_i - n_e) \tag{7}$$

and the electric field was found from $E = -\nabla \phi$.

2. Nondimensionalization

The equations were solved in non-dimensional form. For brevity, only an outline of the nondimensionalization procedure is given here. Global reference quantities were chosen for length L_R, velocity u_R, number density n_R, potential ϕ_R, collision rate ν_R, viscosity μ_{vR}, and thermal conductivity k_R. For each species, however, there was a different reference density $\rho_{Rs} = m_s n_R$, temperature $T_{Rs} = m_s u_R^2 / k_B$, and pressure $p_{Rs} = m_s n_R u_R^2$. Space charge was normalized by the electron charge e, and heat of formation was normalized by $m_s u_R^2$.

The nondimensionalized equations have much the same form as (1)-(7). In addition to a Reynolds number and Prandtl number for each species, the following nondimensional parameters appeared as a consequence of this form of nondimensionalization:

$$\Phi_s = \frac{e\phi_R}{m_s u_R^2} \quad C = \frac{\nu_R L_R}{u_R} \quad a = L_R\sqrt{\frac{en_R}{\epsilon_0 \phi_R}}$$

The nondimensional parameters are, respectively, a relative field strength, a nondimensional collision frequency parameter, and a non-neutrality parameter.

B.   Numerical Methods

The governing equations (1)-(6) were solved using a fourth-order accurate, low-storage Runge-Kutta time marching scheme combined with either a compact spatial difference scheme, Steger-Warming flux splitting, or Roe flux difference splitting. The compact formalism was evaluated with second- through sixth-order accurate differencing, whereas the upwind schemes employed third-order upwind biased differencing in the MUSCL formalism. For the compact scheme, stability was enforced by filtering, typically with a filter of two orders greater than the accuracy of the basic scheme. The Poisson equation (7) was solved by an iterative scheme (described below), with either central or compact spatial differences. The Poisson solution was not filtered. The metric terms were evaluated with central or compact differencing of an order corresponding to the basic scheme.

1.   Governing Equations

In transformed coordinates, the conservation laws (1) can be written in the form:

$$\frac{\partial U}{\partial t} + \frac{\partial E}{\partial \xi} + \frac{\partial F}{\partial \eta} = \frac{\partial E_v}{\partial \xi} + \frac{\partial F_v}{\partial \eta} + S \tag{8}$$

where U is the vector of conserved variables, E and F are the inviscid flux vectors, E_v and F_v are the viscous flux vectors, and S represents the source terms. A standard, low-storage, fourth-order Runge-Kutta scheme[35] was used for time integration of Eq. (8). Three different schemes were used to evaluate the spatial differences: either a compact difference scheme of up to sixth-order accuracy (described below), the Steger-Warming flux split scheme, or the Roe flux difference split scheme. The upwind schemes used third-order MUSCL extrapolation[36] for the inviscid fluxes and second-order central differencing for the viscous terms.

The Poisson equation (7) was solved at the end of each stage of the Runge-Kutta time-integration. It can be written in the following form in transformed coordinates:

$$\frac{\partial E}{\partial \xi} + \frac{\partial F}{\partial \eta} = S_\phi \tag{9}$$

An iteration procedure was introduced such that the potential at iteration step m was $\phi^{m+1} = \phi^m + \Delta\phi$. With a linear expansion about the solution from the previous iteration, and approximate factoring of the implicit terms, the discretized equation has the form:

$$[1 - \Delta\tau(\delta_\xi A \delta_\xi - D)] [1 - \Delta\tau \delta_\eta B \delta_\eta] \Delta\phi = \omega\Delta\tau \left[\frac{\partial E^m}{\partial \xi} + \frac{\partial F^m}{\partial \eta} - S_\phi^m\right] \tag{10}$$

with iteration driving $\Delta\phi$ to zero. Here A and B are flux Jacobians, D is the source Jacobian, τ is a time-like variable introduced to motivate the iteration process, and ω is an over-relaxation factor. Discretizing the left-hand side using second order central differences in space, a tridiagonal system of equations is obtained. (Since iteration drives $\Delta\phi$ to zero, the form of the discretization of the left-hand-side does not affect the order of spatial accuracy of the converged solution.) Either central or compact difference schemes were used to evaluate the spatial differences present on the right hand side of Eq. (10), and the system was solved using the Thomas tridiagonal algorithm.[37] The pseudo-time-step $\Delta\tau$ was varied cyclically to accelerate convergence, and iteration was continued until the change in potential $\Delta\phi$ had dropped below a specified tolerance.

2. Compact Differences

Considering a one-dimensional, uniform mesh, the following central difference scheme[6,7] with a 5-point stencil can be used to generate estimates of the first derivative $\phi'_i = \partial\phi/\partial x|_{x_i}$ with up to sixth-order accuracy:

$$\alpha\phi'_{i-1} + \phi'_i + \alpha\phi'_{i+1} = a\frac{\phi_{i+1} - \phi_{i-1}}{2\,\Delta x} + b\frac{\phi_{i+2} - \phi_{i-2}}{4\,\Delta x} \tag{11}$$

Here α, a, and b are constants that are used to alter the properties of the scheme, and $\phi(x)$ is a generic function, not to be confused with the electric potential. Taylor series expansions can be used to derive a family of second- to sixth-order accurate schemes employing this template.[6,7] Table 1 gives selected coefficients for internal points using Eq. (11) for different orders of accuracy. Note that the implicit form of the scheme ($\alpha \neq 0$) results in a narrower stencil for a given order of accuracy than for an explicit form ($\alpha = 0$). Modified schemes[7] were used near boundaries, where the interior stencil would protrude outside of the domain.

Table 2 shows the forms of the compact difference scheme that were examined in this project, using the notation of Gaitonde and Visbal. To evaluate the derivative at each point, the appropriate form of Eq. (11) was solved using the Thomas tridiagonal algorithm.[37] Second derivatives were evaluated by applying the differencing scheme twice.

Numerical stability was enforced using filtering, typically with a filter of two orders greater than the accuracy of the basic scheme. The form of the filtering scheme[7] for interior points was as follows:

$$\alpha_f\overline{\phi}_{i-1} + \overline{\phi}_i + \alpha_f\overline{\phi}_{i+1} = \sum_{n=0}^{N}\frac{a_n}{2}(\phi_{i+n} + \phi_{i-n}) \tag{12}$$

where $\overline{\phi}_i$ is the filtered value of ϕ_i, and $N+1$ is the order of the filter. A table of coefficients for interior-point filters of second to eighth order is given in Table 3. Modified filters were used near the boundaries; the various options are shown in Table 2. (In the table, F0 indicates that no filter was applied to the boundary points.) The filter was applied to the conserved variables at the end of a time step, and the boundary conditions were updated so that the boundary points were consistent with the filtered interior points. For the cases labeled Filter A in Table 2, the filter's free parameter was set to $\alpha = 0.40$, whereas for Filter B, the value was varied between $\alpha = 0.495$ at the boundary and $\alpha = 0.400$ for the interior points.

III. Results

Sample compact difference calculations are presented here for several test cases, including a Poisson equation solution, a compressible Couette flow problem, a hypersonic laminar boundary layer flow, and a transient plasma-sheath problem. Accuracy is evaluated for second- through sixth-order compact schemes, and compared to standard second-order upwind schemes.

A. Poisson Solver Test

To verify the correct implementation of the Poisson solver, the code was tested against the following problem:

$$\frac{\partial^2\phi}{\partial x^2} + \frac{\partial^2\phi}{\partial y^2} = xe^y \tag{13}$$

with $\phi = xe^y$ imposed on the boundary of the domain. The analytical solution for this problem is $\phi(x,y) = xe^y$.

Calculations were carried out with the compact difference schemes 1-5 in Table 2, and compared to calculations using a second-order central difference scheme. For each case, the solver was run for 10^5 iterations to ensure convergence to machine precision.

Sample results are shown in Fig. 1 for a 31×31 computational mesh (see Fig. 1a). The mesh is deliberately distorted to test the correct implementation of the metric terms. The solution obtained with Compact Scheme 5 is shown in Fig. 1b. The value of the potential rises smoothly from zero at the origin to about 2.7 at the upper right corner of the domain. The absolute error is shown, respectively, for the compact and central difference schemes in Figs. 1c-d. The maximum absolute error for the compact scheme was 6.3×10^{-6}, whereas the corresponding error for the central scheme was 1.3×10^{-2}.

The iterative convergence rate of of the two schemes is examined in Fig. 2a. The maximum change in the potential is plotted as a function of iteration number. Oscillations appear in the plots because of the cyclic variation of the pseudo-time parameter. The envelope of the curves drops almost linearly on these semi-log plots. Eventually, the limit of machine precision is reached, and the value levels off. The solution converged more slowly with the compact scheme, probably because the left-hand-side of Eq. (10) was evaluated using a second-order central difference framework. This issue will be addressed in future work.

Figure 2b shows the maximum error for each numerical scheme as a function of mesh size for grids between 11×11 and 161×161. The slope of the lines on the log-log plot follows the expected value for the order of the scheme. (Each curve is a power-law fit to the points, and is annotated with the absolute value of its exponent.) Generally, the compact schemes show better absolute accuracy than corresponding explicit numerical schemes of the same order. The second-order scheme in the compact formalism has higher absolute accuracy than the conventional central scheme. The difference between these two cases lies in the manner in which the second derivative is evaluated (conventional vs. first derivative applied twice).

B.   Compressible Couette Flow

As a test of the diffusion terms in the conservation laws, computations were carried out for a compressible Couette flow problem. A single species of neutral gas was assumed. This problem has a similar nature to the Poisson solver test, but includes the effects of variable transport properties, so is weakly non-linear. Further, the steady-state solution is obtained through time-marching, rather than iteration.

The problem consists of a thin layer of gas between two walls, one moving and one stationary, which are separated by a distance H. The lower wall $(y = 0)$ is labeled 1, and the upper wall $(y = H)$ is labeled 2. The boundary conditions are:

$$
\begin{aligned}
u(x,0) &= 0 & T(x,0) &= T_1 \\
u(x,H) &= u_2 & T(x,H) &= T_2
\end{aligned}
\tag{14}
$$

with $\partial/\partial x = 0$. The Prandtl number was assumed to be $\mathrm{Pr} = 0.72$ and the viscosity was assumed to vary linearly with temperature. This problem has the following analytical solution:

$$
y^* = \frac{2u^* \left[T_1^* + \frac{1}{2}\left(1 - T_1^*\right)u^* + \mathrm{Pr}\frac{\gamma-1}{2}M^2 \left(\frac{1}{2}u^* - \frac{1}{3}u^{*2}\right)\right]}{1 + T_1^* + Pr\frac{\gamma-1}{6}M^2}
$$

$$
T^* = T_1^* + \left(1 - T_1^*\right)u^* + \mathrm{Pr}\frac{\gamma-1}{2}M^2 \left(u^* - u^{*2}\right)
\tag{15}
$$

where $M = u_2/a_2$, $y^* = y/H$, $u^* = u/u_2$, and $T^* = T/T_2$.

Sample calculations were carried out for $M = 2$ and $T_1/T_2 = 2$, exercising only the neutral-gas module in the computer code. Filter A of Table 2 was used for these computations. Solution profiles are shown in Fig. 3a, where the analytical solution is compared to the numerical solution with Compact Scheme 5 on a 9×11 point mesh. The results computed with this high-order scheme are seen to match the analytical solution closely even for this course mesh. For the incompressible case $(M = 0)$, both profiles would be linear; see Eq. (15). A moderate temperature rise due to dissipation is evident for this Mach 2 flow, and there is a corresponding distortion of the velocity profile.

The results of a grid convergence study are shown in Fig. 3b for each of the spatial differencing schemes of Table 2. Grids of 11, 21, 41, and 81 points in the y-direction were employed. Each of the schemes is seen to converge at rate close to its theoretical order of accuracy. (Each curve is annotated with the exponent of the power-law curve fit.) Interestingly, the mixed fourth and sixth order scheme is almost as accurate as the full sixth-order scheme for this problem. This high accuracy is probably a consequence of the mesh clustering near the boundaries that was employed for these test cases.

C.   Hypersonic Boundary Layer

As a full test of the basic fluid solver, computations were carried out for a Mach 6, laminar boundary layer flow in air. The thermophysical properties of air were taken from White,[34] and the modules for the Poisson equation and charged particle motion were turned off in the code. The Reynolds number, based on plate length, was $\mathrm{Re}_L = 1.8 \times 10^5$. An adiabatic wall boundary condition was chosen in order to introduce a strong hypersonic interaction effect.

American Institute of Aeronautics and Astronautics

The computational grid consisted of 101×101 points, with clustering near the wall and leading edge. Three numerical schemes were employed: Roe, Steger-Warming, and a mixed scheme with fourth-order compact differencing used in smooth regions and the Roe scheme employed where a shock was detected. Filter B of Table 2 was used for these computations.

The procedure for handling shocks with the compact scheme was largely based on the work of Visbal and Gaitonde.[38] Briefly, a simple, thresholded pressure-field smoothness switch was used to identify certain cells as containing a shock. The pressure field is shown in Fig. 4a, and the shock locations identified by the pressure switch are shown in Fig. 4b. The filter scheme was smoothly blended between no filtering at a shock, and full sixth-order filtering in regions of smooth solution away from shocks. Analogously, the scheme was blended between the Roe scheme at the shock and the full fourth-order compact scheme in smooth regions.

Velocity and temperature profiles obtained with each scheme are compared to a similarity solution corresponding to the local edge Mach number in Fig. 5a. Because of the streamwise pressure gradient caused by the hypersonic leading edge interaction effect, exact similarity does not exist for this flow. Nevertheless, reasonable agreement is obtained between the numerical results and the similarity solution. The three numerical schemes are seen to agree fairly closely.

Skin friction and recovery factor profiles provide a more challenging test of the accuracy of the numerical scheme, as shown in Fig. 5b. All three schemes agree closely for the recovery factor. The Roe and mixed compact schemes agree closely for the skin friction, but the highly dissipative (unmodified) Steger-Warming scheme does not accurately capture this property.

D.   Transient Sheath

As a test of the coupled moment equations and Poisson equation, a two-dimensional transient sheath problem was considered, investigating the effect of a suddenly-applied voltage on an initially-uniform, low-density plasma in an annular domain. A similar transient sheath problem has been used as a one-dimensional test case in previous papers.[39, 40]

A three-moment model was considered for this problem. The ion properties were computed using the conservation laws (1), whereas the electron temperature was held fixed at $T_e = 11600$ K and the electron number density was computed by assuming Boltzmann equilibrium: $n_e = n_0 \exp(e\phi/k_B T_e)$. Both inelastic and elastic collisions were included in the computation, but ionization was negligible for the conditions examined here. The neutral background gas was assumed to be at rest with a temperature of 300 K and a pressure of 0.07 Pa.

A sample 101×101 computational mesh is shown in Fig. 6a. The spatial coordinates are nondimensionalized by the electron Debye length $\lambda_D = \sqrt{\epsilon_0 k_B T_e/(n_0 e^2)}$. An O-type mesh was employed, with 5 points of overlap in the circumferential direction.

The initial condition was taken to be a stationary, uniform plasma of number density $n_0 = 1 \times 10^{14}$ m^{-3} and temperature $T_i = 300$ K, and a potential of $\phi = -50$ V was suddenly applied at the inner electrode $(r = 100\lambda_D)$ at time $t = 0$. The potential at the outer boundary of the computational domain was held fixed at zero. Ion properties at the outer boundary were held fixed, while extrapolation consistent with each numerical scheme and supersonic ion outflow was used at the inner boundary.

The ionized gas has the following response to the change in boundary conditions. With the sudden application of a negative potential, the electrons are repelled from the electrode, forming a layer of positive charge. The relatively massive ions slowly respond to the changed conditions, forming an ion current into the electrode. As a result, the space charge diminishes, and the sheath expands. Ahead of the sheath, a quasi-neutral presheath propagates into the bulk plasma as an expansion wave.

Figure 6b shows the distribution of ion number density at $\omega_{pi}t = 18$, where $\omega_{pi} = \sqrt{n_o e^2/(\epsilon_0 m_i)}$. Corresponding radial profiles are shown in Figs. 7a-b, and the time-history of the ion current density at the inner electrode is shown in Fig. 7c. Here, number density is nondimensionalized by the initial plasma density n_0, the velocity is nondimensionalized by the the Bohm velocity $u_B = \sqrt{k_B T_e/m_i}$, and the temperature is nondimensionalized by the electron temperature T_e.

The space charge layer is evident for the approximate range $100 \leq r \leq 130$, and a large corresponding potential drop is evident (Fig. 7a). The large electric field there leads to high ion velocities, and high ion temperatures brought about by the dissipative effects of elastic ion-neutral collisions (Fig. 7b).

The time-evolution of the ion current density $j_i = e n_i |u_i|$ at the inner electrode is shown in Fig. 7c. The time-axis is shown on a logarithmic scale to illustrate the solution details more clearly. There is an initial surge in current as the transient sheath forms, followed by a gradual relaxation to constant current density

American Institute of Aeronautics and Astronautics

at large times. In this asymptotic state, the current to the electrode is balanced by ions uncovered by the expanding rarefaction wave. The presheath accelerates the ions up to approximately the Bohm velocity, supporting a quasi-steady sheath.

As a gauge of the quality of the solution for different numerical schemes, the ion current at the inner electrode for $\omega_{pi}t = 18$ was examined. The error in this quantity, relative to a reference solution of 101×101 points using Compact Scheme 5, is plotted versus grid size in Fig. 7d for grids between 41×41 and 71×71 points. Again, each power-law curve fit is annotated with its exponent, and the slope of the lines on the log-log plot follows the expected value for the order of the scheme. These results show that compact difference methods of up to sixth order can successfully achieve their theoretical order of accuracy for the coupled Poisson and Euler equations with source terms. It should be noted that spatial convergence tends to degenerate to second order if the Poisson solution is not tightly converged for each time step.

IV.   Summary and Conclusions

This paper has explored the feasibility of applying high-order, compact difference methods to the modeling of glow discharges for high-speed flow control. High-order compact difference methods offer a possible means of achieving high spatial accuracy on coarser grids, potentially leading to a significant reduction in computational cost. Two-dimensional compact difference calculations were carried out for several test cases, including a Poisson equation solution, a compressible Couette flow problem, a hypersonic laminar boundary layer flow, and a transient plasma-sheath problem. Spatial convergence of second- through sixth-order compact schemes was investigated, and found to be comparable to the theoretical order of accuracy. In particular, compact difference methods of up to sixth order can successfully achieve their theoretical order of accuracy for the coupled Poisson and Euler equations with source terms. Compact difference schemes appear to be a promising numerical approach for modeling plasma actuators for high-speed flow control. Future work will focus on shock capturing and on more complex discharge problems.

Acknowledgments

References

[1]Surzhikov, S. T. and Shang, J. S., "Two-Component Plasma Model for Two-Dimensional Glow Discharge in Magnetic Field," *Journal of Computational Physics*, Vol. 199, 2004, pp. 437–464.

[2]Mahadevan, S. and Raja, L. L., "Simulations of Glow Discharge Phenomena in Air for High-Speed Flow Control," AIAA Paper 2008-1093, American Institute of Aeronautics and Astronautics, Reston VA, January 2008.

[3]Poggie, J., "Numerical Simulation of Direct Current Glow Discharges for High-Speed Flow Control," *Journal of Propulsion and Power*, Vol. 24, No. 5, 2008, pp. 916–922.

[4]Poggie, J., "Numerical Simulation of DC and RF Glow Discharges," AIAA Paper 2007-0632, American Institute of Aeronautics and Astronautics, Reston VA, January 2007.

[5]Poggie, J., "Discharge Modeling for Flow Control Applications," AIAA Paper 2008-1357, American Institute of Aeronautics and Astronautics, Reston VA, January 2008.

[6]Lele, S. K., "Compact Finite Difference Schemes with Spectral-Like Resolution," *Journal of Computational Physics*, Vol. 103, 1992, pp. 16–42.

[7]Gaitonde, D. V. and Visbal, M. R., "High-Order Schemes for Navier-Stokes Equations: Algorithm and Implementation in FDL3D," AFRL Technical Report AFRL-VA-WP-TR-1998-3060, Air Force Research Laboratory, Wright-Patterson Air Force Base, Ohio, 1998.

[8]Poggie, J., "High-Order Compact Difference Methods for Glow Discharge Modeling," AIAA Paper 2009-1047, American Institute of Aeronautics and Astronautics, Reston VA, January 2009.

[9]Ward, A. L., "Effect of Space Charge in Cold-Cathode Gas Discharges," *Physical Review*, Vol. 112, No. 6, 1958, pp. 1852–1857.

[10]Ward, A. L., "Calculations of Cathode-Fall Characteristics," *Journal of Applied Physics*, Vol. 33, No. 9, 1962, pp. 2789–2794.

[11]Boeuf, J.-P., "A Two-Dimensional Model of DC Glow Discharges," *Journal of Applied Physics*, Vol. 63, No. 5, 1988, pp. 1342–1349.

[12]Raizer, Y. P. and Surzhikov, S. T., "Two-Dimensional Structure in a Normal Glow Discharge and Diffusion Effects in Cathode and Anode Spot Formation," *High Temperature*, Vol. 26, No. 3, 1988, pp. 304–311.

[13]Passchier, J. D. P. and Goedheer, W. J., "A Two-Dimensional Fluid Model for an Argon RF Discharge," *Journal of Applied Physics*, Vol. 74, No. 6, 1993, pp. 3744–3751.

[14]Young, F. F., "Two-Dimensional, Self-Consistent, Three-Moment Simulation of RF Glow Discharges," *IEEE Transactions on Plasma Science*, Vol. 21, No. 3, 1993, pp. 312–321.

[15]Hong, M. and Emmert, G. A., "Two-Dimensional Fluid Modeling of Time-Dependent Plasma Sheath," *Journal of Vacuum Science and Technology*, Vol. 12, No. 2, 1994, pp. 889–896.

[16]Sheridan, T. E. and Alport, M. J., "Two-Dimensional Model of Ion Dynamics During Plasma Source Ion Implantation," *Applied Physics Letters*, Vol. 64, No. 14, 1994, pp. 1783–1785.

[17]Georghiou, G. E., Papadakis, A. P., Morrow, R., and Metaxas, A. C., "Numerical Modelling of Atmospheric Pressure Gas Discharges Leading to Plasma Production," *Journal of Physics D: Applied Physics*, Vol. 38, 2005, pp. R303–R328.

[18]Graves, D. B. and Jensen, K. F., "A Continuum Model of DC and RF Discharges," *IEEE Transactions on Plasma Science*, Vol. PS-14, No. 2, 1986, pp. 78–91.

[19]Richards, A. D., Thompson, B. E., and Sawin, H. H., "Continuum Modeling of Argon Radio Frequency Glow Discharges," *Applied Physics Letters*, Vol. 50, No. 9, 1987, pp. 492–494.

[20]Barnes, M. S., Cotler, T. J., and Elta, M. E., "A Staggered-Mesh Finite-Difference Numerical Method for Solving the Transport Equations in Low Pressure RF Glow Discharges," *Journal of Computational Physics*, Vol. 77, 1988, pp. 53–72.

[21]Hammond, E. P., Mahesh, K., and Moin, P., "A Numerical Method to Simulate Radio-Frequency Plasma Discharges," *Journal of Computational Physics*, Vol. 176, 2002, pp. 402–429.

[22]Meyyappan, M. and Kreskovsky, J. P., "Glow Discharge Simulation Through Solutions to the Moments of the Boltzmann Transport Equation," *Journal of Applied Physics*, Vol. 68, No. 4, 1990, pp. 1506–1512.

[23]Meyyappan, M., "A Continuum Model for Low-Pressure Radio-Frequency Discharges," *Journal of Applied Physics*, Vol. 69, No. 12, 1991, pp. 8047–8051.

[24]Widner, M., Alexeff, I., Jones, W. D., and Lonngren, K. E., "Ion Acoustic Wave Excitation and Ion Sheath Evolution," *The Physics of Fluids*, Vol. 13, No. 10, 1970, pp. 2532–2540.

[25]Sternberg, N. and Poggie, J., "Plasma-Sheath Transition in the Magnetized Plasma-Wall Problem for Collisionless Ions," *IEEE Transactions on Plasma Science*, Vol. 32, No. 6, 2004, pp. 2217–2226.

[26]Poggie, J. and Sternberg, N., "Transition from the Constant Ion Mobility Regime to the Ion-Atom Charge-Exchange Regime for Bounded Collisional Plasmas," *Physics of Plasmas*, Vol. 12, No. 2, 2005, pp. 023502–1–023502–9.

[27]Chapman, S. and Cowling, T. G., *The Mathematical Theory of Non-Uniform Gases*, Cambridge University Press, 2nd ed., 1952.

[28]Appleton, J. P. and Bray, K. N. C., "The Conservation Equations for a Non-Equilibrium Plasma," *Journal of Fluid Mechanics*, Vol. 20, No. 4, 1964, pp. 659–672.

[29]Burgers, J. M., *Flow Equations for Composite Gases*, Academic Press, New York, 1969.

[30]Morse, T. F., "Energy and Momentum Exchange between Nonequipartition Gases," *The Physics of Fluids*, Vol. 6, No. 10, 1963, pp. 1420–1427.

[31]Lister, G. G., "Low-Pressure Gas Discharge Modelling," *Journal of Physics D*, Vol. 25, No. 12, 1992, pp. 1649–1680.

[32]Yuan, X. and Raja, L. L., "Computational Study of Capacitively Coupled High-Pressure Glow Discharges in Helium," *IEEE Transactions on Plasma Science*, Vol. 31, No. 4, 2003, pp. 495–503.

[33]Adamovich, I. V., Subramaniam, V. V., Rich, J. W., and Macheret, S. O., "Phenomenological Analysis of Shock-Wave Propagation in Weakly Ionized Plasmas," *AIAA Journal*, Vol. 36, No. 5, 1998, pp. 816–822.

[34]White, F. M., *Viscous Fluid Flow*, McGraw-Hill, New York, 2nd ed., 1991.

[35]Hoffmann, K. A. and Chiang, S. T., *Computational Fluid Dynamics*, Engineering Educational System, Wichita KS, 4th ed., 2000.

[36]Anderson, W. K., Thomas, J. L., and van Leer, B., "A Comparison of Finite Volume Flux Vector Splittings for the Euler Equations," AIAA Paper 85-0122, American Institute of Aeronautics and Astronautics, Reston VA, January 1985.

[37]Cheney, W. and Kincaid, D., *Numerical Mathematics and Computing*, Brooks/Cole Publishing, Pacific Grove, California, 3rd ed., 1994.

[38]Visbal, M. R. and Gaitonde, D. V., "Shock Capturing Using Compact-Differencing-Based Methods," AIAA Paper 2005-1265, American Institute of Aeronautics and Astronautics, Reston VA, January 2005.

[39]Poggie, J. and Gaitonde, D. V., "Electrode Boundary Conditions in Magnetogasdynamic Flow Control," AIAA Paper 2002-0199, American Institute of Aeronautics and Astronautics, Reston VA, January 2002.

[40]Poggie, J., Gaitonde, D. V., and Sternberg, N., "Numerical Simulation of Plasma Sheaths in Aerodynamic Applications," AIAA Paper 2002-2166, American Institute of Aeronautics and Astronautics, Reston VA, May 2002.

| Scheme	α	a	b	Stencil	Order
E2	0	1	0	3	2
E4	0	4/3	-1/3	5	4
C4	1/4	3/2	0	3	4
C6	1/3	14/9	1/9	5	6

Table 1. **Coefficients for compact difference schemes at interior points. Adapted from Gaitonde and Visbal.**[7]

	Scheme	Filter A	Filter B
0	Conventional Central	F0-FB$_{2,4}$-F4-FB$_{2,4}$-F0	F0-F2-F4-F2-F0
1	E2-DE2-E2-DE2-E2	F0-FB$_{2,4}$-F4-FB$_{2,4}$-F0	F0-F2-F4-F2-F0
2	E4-DE4-E4-DE4-E4	F0-FB$_{2,6}$-FB$_{3,6}$-F6-FB$_{3,6}$-FB$_{2,6}$-F0	F0-F2-F4-F6-F4-F2-F0
3	E4-AC4-C4-AC4-E4	F0-FB$_{2,6}$-FB$_{3,6}$-F6-FB$_{3,6}$-FB$_{2,6}$-F0	F0-F2-F4-F6-F4-F2-F0
4	E4-AC4-C6-AC4-E4	F0-FB$_{2,6}$-FB$_{3,8}$-FB$_{4,8}$-F8-FB$_{4,8}$-FB$_{3,8}$-FB$_{2,6}$-F0	F0-F2-F4-F6-F8-F6-F4-F2-F0
5	E6-AC6-C6-AC6-E6	F0-FB$_{2,8}$-FB$_{3,8}$-FB$_{4,8}$-F8-FB$_{4,8}$-FB$_{3,8}$-FB$_{2,8}$-F0	F0-F2-F4-F6-F8-F6-F4-F2-F0

Table 2. **Compact difference schemes and corresponding filters. Notation of Gaitonde and Visbal.**[7]

Scheme	a_0	a_1	a_2	$a3$	a_4	Order
F2	$\frac{1+2\alpha_f}{2}$	$\frac{1+2\alpha_f}{2}$	0	0	0	2
F4	$\frac{5+6\alpha_f}{8}$	$\frac{1+2\alpha_f}{2}$	$\frac{-1+2\alpha_f}{8}$	0	0	4
F6	$\frac{11+10\alpha_f}{16}$	$\frac{15+34\alpha_f}{32}$	$\frac{-3+6\alpha_f}{16}$	$\frac{1-2\alpha_f}{32}$	0	6
F8	$\frac{93+70\alpha_f}{128}$	$\frac{7+18\alpha_f}{16}$	$\frac{-7+14\alpha_f}{32}$	$\frac{1-2\alpha_f}{16}$	$\frac{-1+2\alpha_f}{128}$	8

Table 3. **Coefficients for filter schemes at interior points. Adapted from Gaitonde and Visbal.**[7]

American Institute of Aeronautics and Astronautics
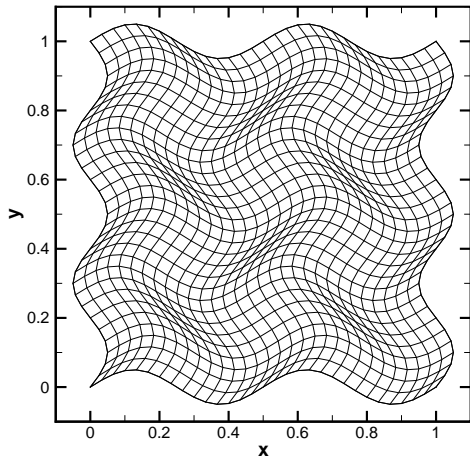
(a) Computational mesh.
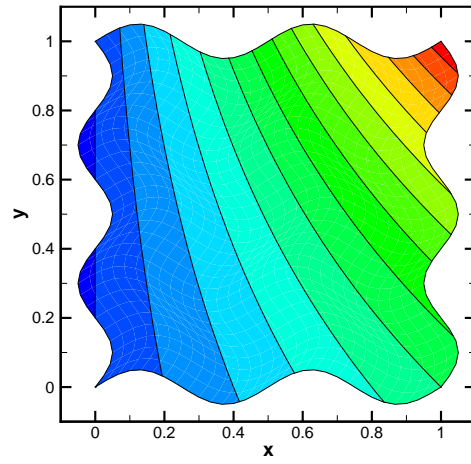
(b) Solution computed with Compact Scheme 5.
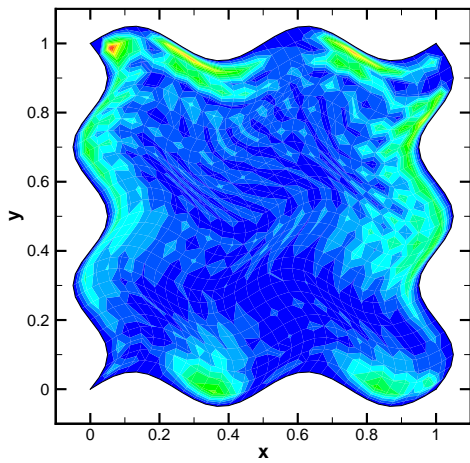
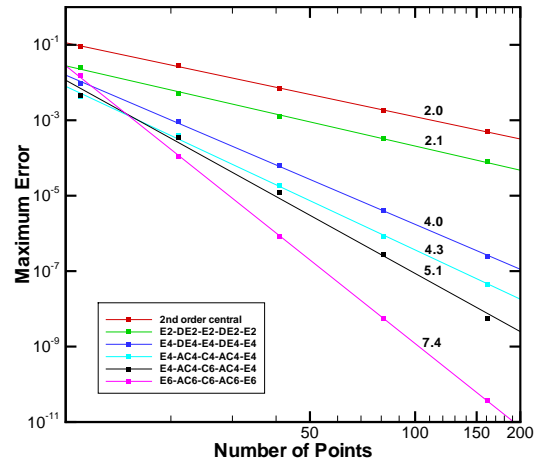(c) Absolute error, Compact Scheme 5 (contour 1×10^{-6}).
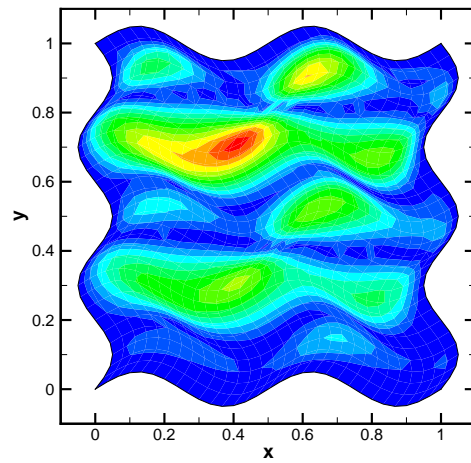
(d) Absolute error, central scheme (contour 1×10^{-3}).

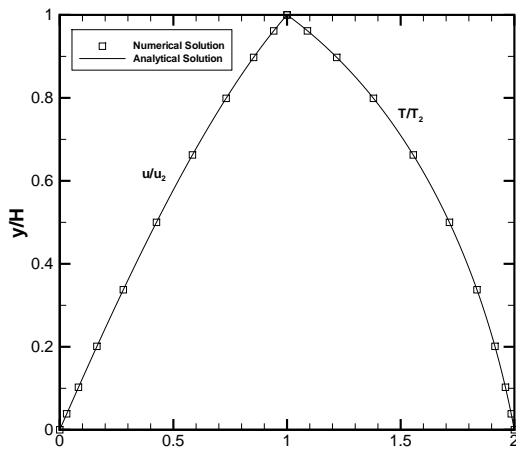**Figure 1. Test of Poisson solver, 31×31 grid.**
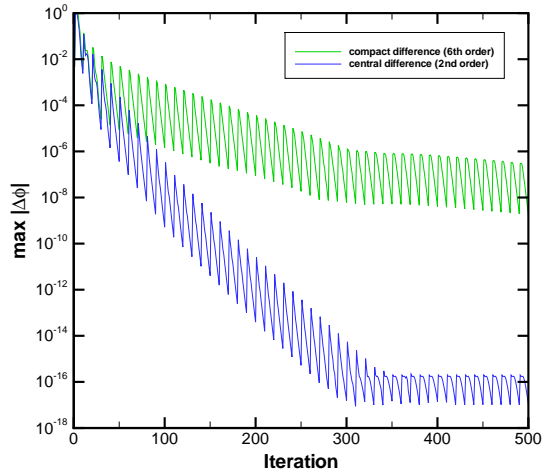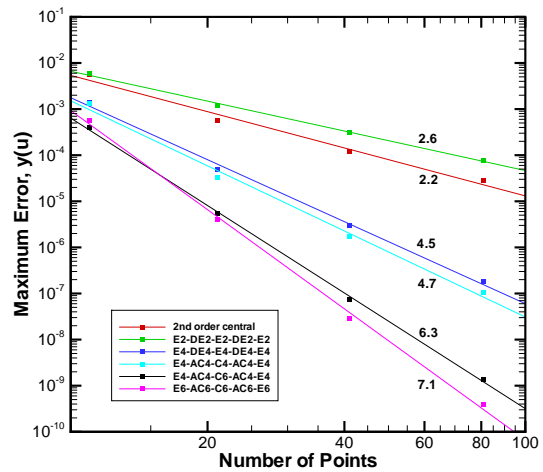
(a) Iterative convergence, 31×31 grid.

(b) Spatial convergence. Annotated with exponent of power law fit.
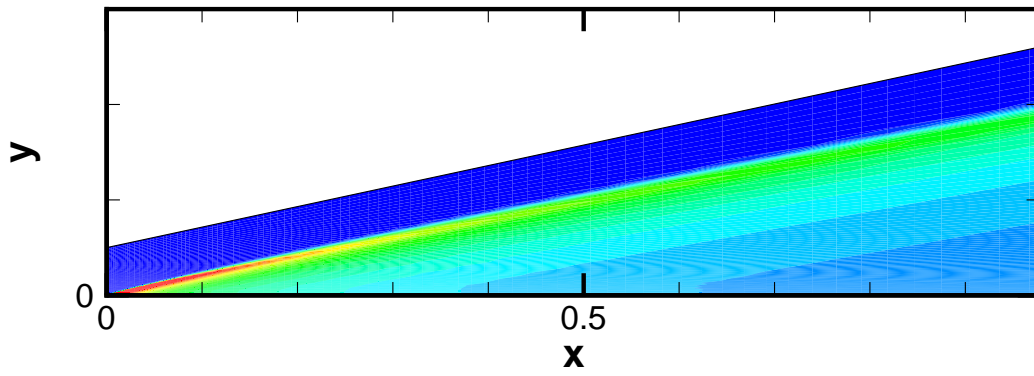
Figure 2. Convergence of Poisson solution.
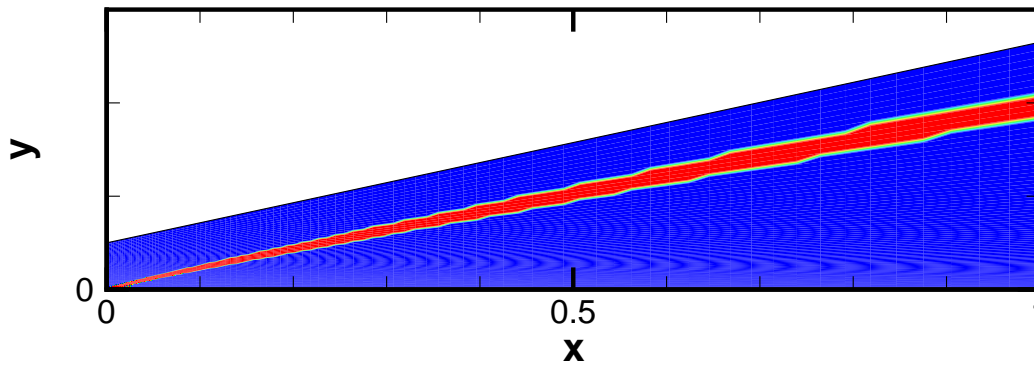

(a) Velocity and temperature profiles (Compact Scheme 5, 9×11 point mesh).

(b) Spatial convergence, refinement in y-direction. Annotated with exponent of power law fit.

Figure 3. Compressible Couette flow test case ($M = 2$, $T_1/T_2 = 2$).

American Institute of Aeronautics and Astronautics

(a) Pressure field.

(b) Shock location.

Figure 4. Shock detection for laminar, Mach 6 boundary layer solution.
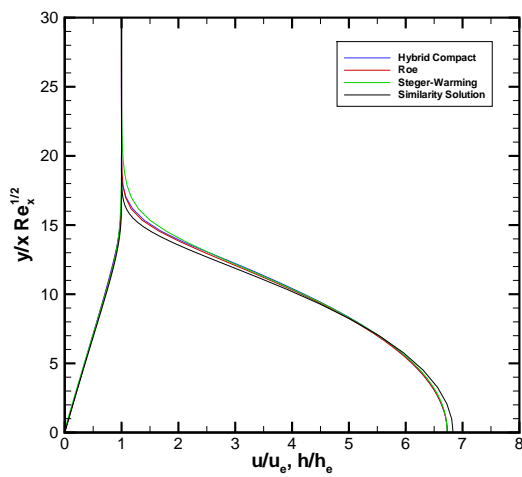
(a) Boundary layer profiles ($M_e = 5.9$).
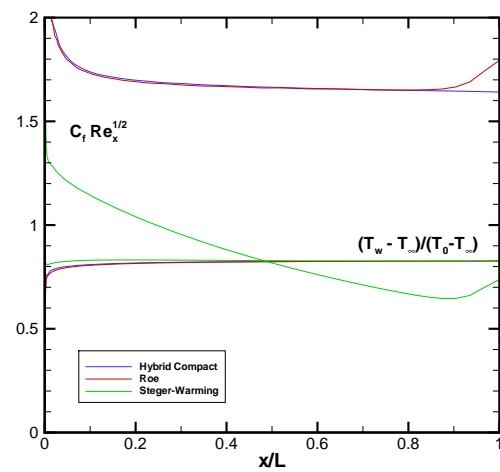
(b) Skin friction and recovery factor profiles.

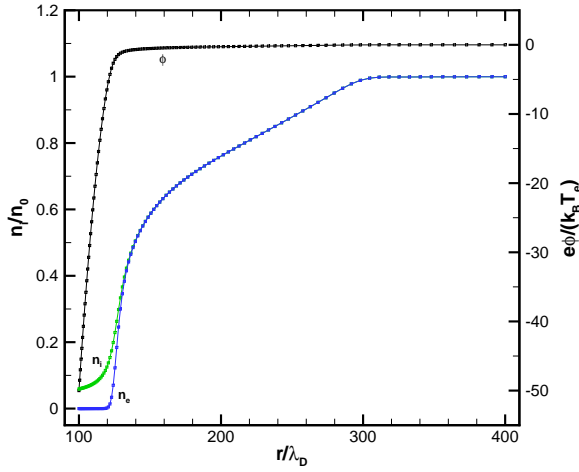**Figure 5. Laminar, Mach 6 boundary layer solution.**
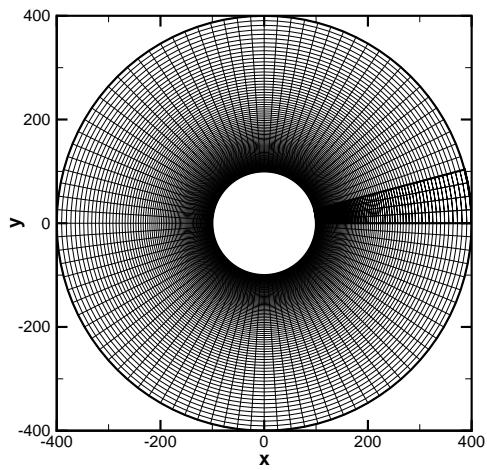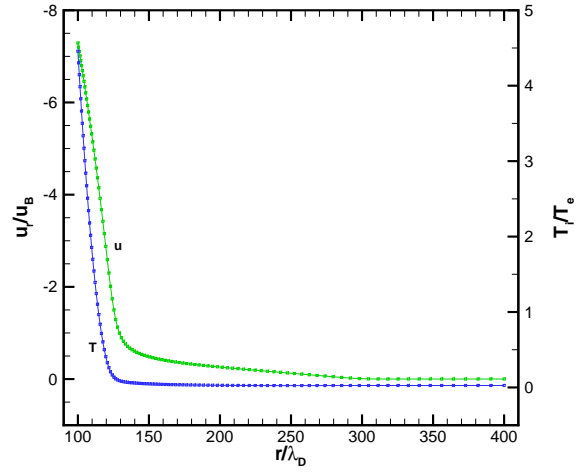
(a) Computational mesh (101×101 points).
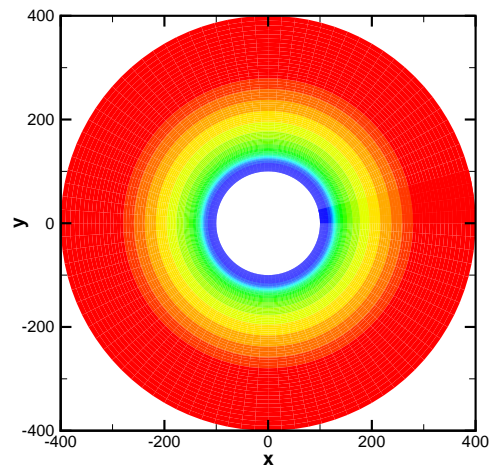
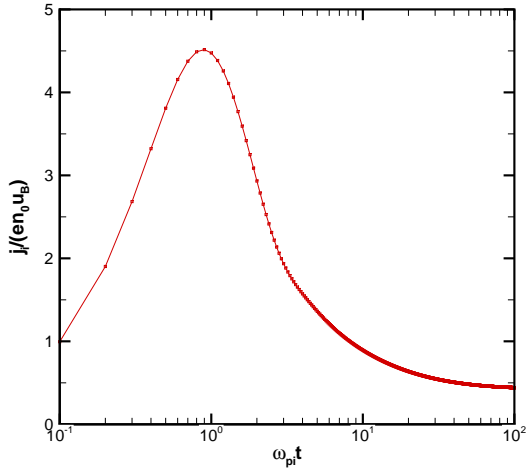(b) Ion number density, $\omega_{pi}t = 18$, Compact Scheme 5.
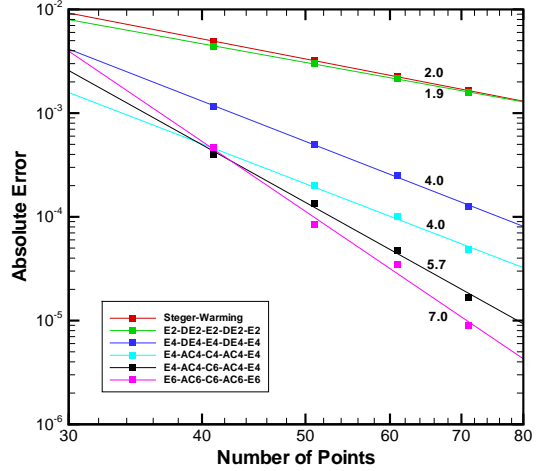
Figure 6. Transient sheath test case.

(a) Radial profile, $\omega_{pi}t = 18$, Compact Scheme 5.

(b) Radial profile, $\omega_{pi}t = 18$, Compact Scheme 5.

(c) Ion current, $r/\lambda_D = 100$, Compact Scheme 5.

(d) Spatial convergence. Annotated with exponent of power law fit.

Figure 7. Transient sheath test case.